High-fidelity quantitative differential phase contrast deconvolution using dark-field sparse prior

PROCEEDINGS OF SPIE

SPIEDigitalLibrary.org/conference-proceedings-of-spie

High-fidelity quantitative differential phase contrast deconvolution using dark-field sparse prior

Shuhe Zhang, Tao Peng, Zeyu Ke, Meng Shao, Tos T. J. Berendschot, et al.

Shuhe Zhang, Tao Peng, Zeyu Ke, Meng Shao, Tos T. J. M. Berendschot, Jinhua Zhou, "High-fidelity quantitative differential phase contrast deconvolution using dark-field sparse prior," Proc. SPIE 12745, Sixteenth International Conference on Photonics and Imaging in Biology and Medicine (PIBM 2023), 127450X (18 July 2023); doi: 10.1117/12.2683923

SPIE.

Event: Sixteenth International Conference on Photonics and Imaging in Biology and Medicine (PIBM 2023), 2023, Haikou, China

High-fidelity quantitative differential phase contrast deconvolution using dark-field sparse prior

Shuhe Zhang[a,b,*], Tao Peng,[a] Zeyu Ke[a], Meng Shao[a], Tos T. J. M. Berendschot[b], Jinhua Zhou[a,c,**]

[a]School of Biomedical Engineering, Anhui Medical University, Hefei 230032, China; [b]University Eye Clinic Maastricht, Maastricht University Medical Center + , P.O. Box 5800, Maastricht, 6202 AZ, the Netherlands; [c]Anhui Provincial Institute of Translational Medicine, Anhui Medical University, Hefei 230032, China.

ABSTRACT

Differential phase contrast (DPC) imaging plays an important role in the family of quantitative phase measurement. However, the reconstruction algorithm for quantitative DPC (qDPC) imaging is not yet optimized, as it does not incorporate the inborn properties of qDPC imaging. In this research, we propose a simple but effective image prior, the dark-field sparse prior (DSP), to facilitate the phase reconstruction quality for all DPC-based phase reconstruction algorithms. The DSP is based on the key observation that most pixel values for an idea differential phase contrast image are zeros since the subtraction of two images under anti-symmetric illumination cancels all background components. With this DSP prior, we formed a new cost function in which L_0-norm was used to represent the DSP. Further, we developed the algorithm based on the Half Quadratic Splitting to solve this NP-hard L_0-norm problem. We tested our new model on both simulated and experimental data and compare it against state-of-the-art (SOTA) methods including L_2-norm and total variation regularizations. Results show that our proposed model is superior in terms of phase reconstruction quality and implementation efficiency, which significantly increases the experimental robustness, while maintaining the data fidelity. In general, the DSP supports high-fidelity qDPC reconstruction without any modification of the optical system, which simplifies the system complexity and benefit all qDPC applications.

Keywords: Differential phase contrast; dark-field sparse prior; L_0-norm; Half Quadratic Splitting.

1. INTRODUCTION

Quantitative differential phase-contrast microscopy (qDPC), a non-interferometric quantitative phase retrieval approach, has been used for label-free and stain-free optical imaging of live biological specimens both *in vitro* [1-6] and *in vivo* [7, 8]. A quantitative DPC experimental layout involves a 4-f microscopy system in which a programmable LED or LCD illumination source generates anti-symmetric illumination patterns [6, 9]. With the combination of oblique plane wave illumination and low-pass filtering of the objective lens, the DPC converts the unmeasurable sample phase into a phase-contrast intensity image. By collecting at least 4 phase-contrast images with asymmetric illuminations in opposite directions, the phase component of the sample can be reconstructed through a non-blind deconvolution process, where the convolution kernel, in an ideal condition, is defined by the Fourier transform of phase contrast transfer function (PTF) [6]. The spatial deconvolution is then transformed into Fourier space division operation.

However, since no optical system is perfect, qDPC raw images are always corrupted by noise, illumination fluctuations, and optical aberrations, resulting in the degeneration of the phase recovery results since the deconvolution for qDPC phase reconstruction is ill-conditioned: a small change in input leads to a large change in the output.

To tackle the impact of noise and illumination fluctuations, and so improve the reconstruction quality of qDPC deconvolution, in this research, we propose a high-fidelity qDPC reconstruction algorithm in which the dark-field sparse prior (DSP) is proposed and embedded. The DSP is based on the key observation that most pixel values for an idea differential phase contrast image are zeros since the subtraction of two images under anti-symmetric illumination cancels all background components.

Sixteenth International Conference on Photonics and Imaging in Biology and Medicine (PIBM 2023), edited by Qingming Luo, Lihong V. Wang, Valery V. Tuchin, Proc. of SPIE Vol. 12745, 127450X
 · 0277-786X · doi: 10.1117/12.2683923

2. DARK-FIELD SPARSE PRIOR

The dark-field sparse prior is based on a proposition of DPC data that (1) the DPC image is a sparse matrix, and (2) the sparsity of an idea noise-free DPC image is greater than noise-corrupted DPC images (as shown in Fig. 1).

To better illustrate this observation, we consider the point spread function h_n of the differential phase contrast image $\boldsymbol{s}_{n,dpc}$, which is given by

$$h_n(\boldsymbol{x}) = \mathcal{F}^{-1}\left[H_{ph,n}(\boldsymbol{k})\right], \tag{1}$$

where $\mathcal{F}^{-1}$ is the inverse Fourier transform. $\boldsymbol{k}$ is the coordinate vector in Fourier space. $H_{ph,n}(\boldsymbol{k})$ is the contrast phase transform function (PTF) and is determined by [6]

$$H_{ph,n}(\boldsymbol{k}) = i \cdot \iint P(\boldsymbol{k}_{ill})\left[S(\boldsymbol{k}_{ill})P(\boldsymbol{k}_{ill}+\boldsymbol{k}) - S(\boldsymbol{k}_{ill})P(\boldsymbol{k}_{ill}-\boldsymbol{k})\right]\mathrm{d}^2\boldsymbol{k}_{ill}, \tag{2}$$

where $\boldsymbol{k}_{ill}$ is the coordinate vector in the illumination pupil plane. $S(\boldsymbol{k})$ is the illumination pupil and is a pure-real function. $P(\boldsymbol{k})$ for an idea objective lens is a pure-real even function. Let $\boldsymbol{k} = -\boldsymbol{k}$ in Eq. (4) we obtain $H_{ph,n}(\boldsymbol{k}) = -H_{ph,n}(-\boldsymbol{k})$. Therefore, $H_{ph,n}$ is an odd function that meets:

$$H_{ph,n}(0) = 0. \tag{3}$$

Furthermore, according to the property of Fourier transform, $h_n(x)$ is a pure-real odd function thus we have

$$\int_{-\infty}^{\infty} h_n(\boldsymbol{x})\mathrm{d}\boldsymbol{x} = 0, \tag{4}$$

which implies the fact that the integration of an arbitrary odd function among a symmetric interval is zero.

The sparsity of $s_{n,dpc}$ can be analyzed from both Eq. (3) and Eq. (4). First, according to Eq. (3), the $H_{ph,n}$ completely removes the direct-current (DC) components in Fourier space which leads to the fact that the absolute value of DPC image has the similar visual performance to that of dark-field images (background is black). Second, according to Eq. (4), convoluting an image using $h_n(x)$ generates a sparse image as the kernel cancels out pixels that have the same values. In conclusion, $s_{n,dpc}$ in an ideal condition is a sparse matrix.

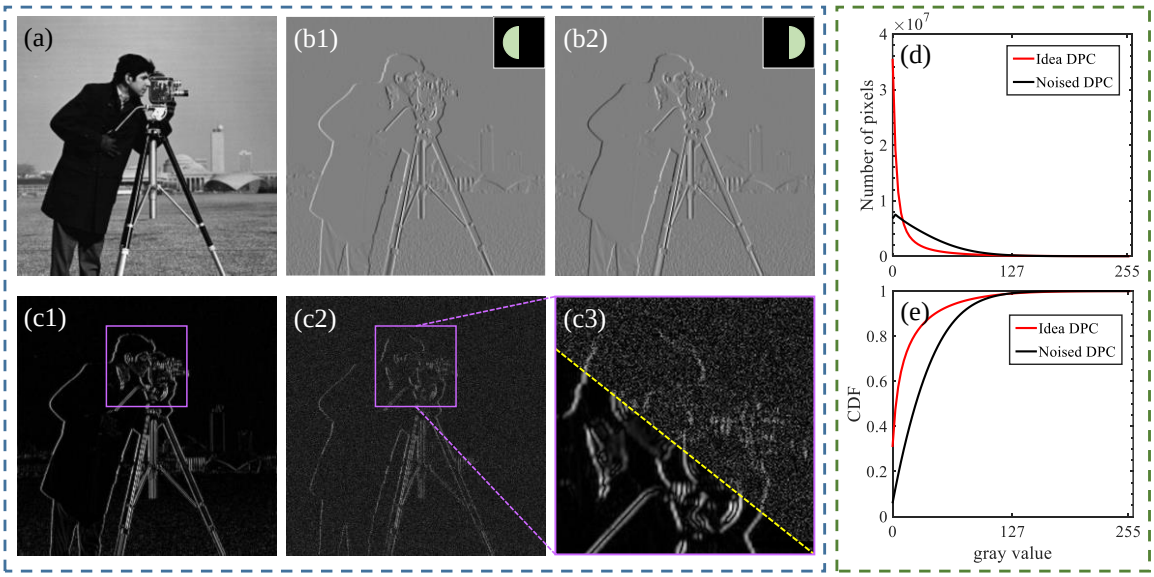

Fig. 1. Simulation of differential phase contrast images. (a) Phase pattern. (b1) and (b2) are simulated image under oblique illumination from left and right, respectively. (c1) is the absolute value of differential phase contrast image of (b1) and (b2). (c2) are the absolute value of (b1) and (b2) when corrupted by noises SNR = 0.7. (c3) enlarged part in the purple box. (d) and (e) are histograms and CDF (Cumulative Distribution Function) for 320 simulated DPC images with and without noise corruption.

The simulated DPC images are shown in Fig. 1. We generate the phase contrast images through simulation as shown in Fig. 1 (b1) and 1 (b2). Their difference pattern is shown in Fig. 1 (c1) in which the pattern is similar to a dark-field image as most of the pixels are zeros. If we add random noise to both Fig. 1 (b1) and 1 (b2), the difference pattern will be shown in Fig. 1 (c2). A partially enlarged image of the purple box is shown in Fig. 1 (c3). Since the noise is random and cannot be canceled by differential operation, the backgrounds where they should be zero are now filled by noise pixels, and the DPC-pattern is not as sparse as the noise-free one.

We also design massive simulations based on different PTFs, and perform statistical analysis shown in Fig. 1 (d) and 1 (e), the idea DPC images are even sparser than noise-corrupted DPC images. We, therefore, are inspired by this sparse observation and propose the dark-field sparse prior (DSP).

Mathematical proofs are as followed: taking L_0-norm on DPC-image, $s_{n,dpc}$, yielding

$$\left\| s_{n,dpc} \right\|_0 = \left\| \frac{I_{n,r} - I_{n,l}}{I_{n,r} + I_{n,l}} \right\|_0 = \left\| I_{n,r} - I_{n,l} \right\|_0 . \tag{5}$$

The L_0-norm counts the nonzero elements of vector (matrix is vectorized) and meets the triangle inequality in which $\|\boldsymbol{A}+\boldsymbol{B}\|_0 \le \|\boldsymbol{A}\|_0 + \|\boldsymbol{B}\|_0$. Since the pixel values in $I_{n,r} + I_{n,l}$ are non-negative, the L_0-norm of $s_{n,dpc}$ equals to the L_0-norm of $\left(I_{n,r} - I_{n,l}\right)$. Let $\varepsilon_{n,r}$ and $\varepsilon_{n,l}$ be the noise signal or uneven background illumination imposed on $I_{n,r}$ and $I_{n,l}$. Since the random noises and uneven background cannot be completely canceled out by the subtraction, we are able to obtain the following inequation

$$\left\| I_{n,r} - I_{n,l} \right\|_0 \le \left\| \left(I_{n,r} + \varepsilon_{n,r}\right) - \left(I_{n,l} + \varepsilon_{n,l}\right) \right\|_0 \le \left\| s_{n,dpc} \right\|_0 + \left\| \varepsilon_{n,r} - \varepsilon_{n,l} \right\|_0 . \tag{6}$$

Equation (6) implies that the presence of noises, uneven background illumination, and illumination fluctuations tends to increase the L_0-norm of $s_{n,dpc}$ since those noises cannot be entirely canceled out during the subtraction. In other words, high-quality DPC image tends to be sparser than those degraded one.

Vectorizing $\boldsymbol{\varphi}$ and $\boldsymbol{s}_{n,dpc}$ within a conventional DPC framework, our sparse-Hessian cost function is defined as,

$$\boldsymbol{\varphi}_{dsp-qDPC} = \arg\min_{\boldsymbol{\varphi}} \sum_{n=1}^{N} \left\| \boldsymbol{K}_n \boldsymbol{\varphi} - \boldsymbol{s}_{n,dpc} \right\|_2^2 + \alpha \sum_{n=1}^{N} \left\| \boldsymbol{K}_n \boldsymbol{\varphi} \right\|_0 + \beta \left\| \mathcal{H} \boldsymbol{\varphi} \right\|_1 , \tag{7}$$

where $\boldsymbol{K}_n$ is the matrix denoting the convolution with kernel $\boldsymbol{h}_n(x)$. The first fidelity term in the augmented Lagrangian Eq. (7) enforces similarity between the convolution result $\boldsymbol{K}_n\boldsymbol{\varphi}$ and the observed DPC images $\boldsymbol{s}_{n,dpc}$. α and β are positive penalty parameters for the following regularization terms and are determined based on the noise level.

The second term is the new proposed DSP involved term aforementioned, and $\boldsymbol{K}_n\boldsymbol{\varphi}$ is the forward model of DPC which can be regarded as generating DPC images with a given estimation of $\boldsymbol{\varphi}$ and $\boldsymbol{K}_n$. The L_0-norm is used to achieve sparsity promotion. The third term is Hessian regularization which can be regarded as higher-order TV regularization. The Hessian regularization uses the second gradient which has a smoother regularization result than that of TV one which uses the first-order gradient. Here $\mathcal{H}$ denotes the Hessian gradient operator.

Since Eq. (7) involves L_0-norm which is a NP-hard problem, we develop two frameworks to approximately tackle the L_0-norm term.

3. HALF QUADRATIC SPLITTING

Equation (7) can be solved by the half quadratic splitting (HQS) algorithm in an alternating manner [10, 11]. By introducing N + 1 auxiliary variables, $\boldsymbol{\psi}_n$, ($n = 1, 2, \cdots, N$) and $\boldsymbol{G}$ with respect to the $\boldsymbol{K}_n\boldsymbol{\varphi}$ and $\mathcal{H}\boldsymbol{\varphi}$ respectively, the problem in Eq. (7) is converted into N + 2 sub-problems which are

$$\begin{cases} \arg\min\limits_{\varphi} \sum\limits_{n=1}^{N} \left\| \boldsymbol{K}_n \boldsymbol{\varphi} - \boldsymbol{s}_{n,dpc} \right\|_2^2 + \alpha_0 \sum\limits_{n=1}^{N} \left\| \boldsymbol{K}_n \boldsymbol{\varphi} - \boldsymbol{\psi}_n \right\|_2^2 + \beta_0 \left\| \mathcal{H} \boldsymbol{\varphi} - \boldsymbol{G} \right\|_2^2 \\ \arg\min\limits_{\boldsymbol{\psi}_n} \alpha_0 \left\| \boldsymbol{K}_n \boldsymbol{\varphi} - \boldsymbol{\psi}_n \right\|_2^2 + \alpha \left\| \boldsymbol{\psi}_n \right\|_0, \quad n = 1,\ 2,\ \cdots N \\ \arg\min\limits_{\boldsymbol{G}} \beta_0 \left\| \mathcal{H} \boldsymbol{\varphi} - \boldsymbol{G} \right\|_2^2 + \beta \left\| \boldsymbol{G} \right\|_1 \end{cases} . \tag{8}$$

Here α_0 and β_0 are sufficient large penalty parameters such that they enforce their corresponding L_2-norm terms approach to zero. For $\boldsymbol{\psi}_n$ sub-problems (L_0-norm), it can be approximately solved by hard-threshold, and the closed-form solution is given by [11]

$$\boldsymbol{\psi}_n = \begin{cases} \boldsymbol{K}_n \boldsymbol{\varphi}, & \sum_{n=1}^{N} \left| \boldsymbol{K}_n \boldsymbol{\varphi} \right|^2 > \alpha / \alpha_0 \\ \boldsymbol{0}, & else \end{cases} . \tag{9}$$

For $\boldsymbol{G}$ sub-problem (L_1-norm), it is solved by the soft-threshold and the closed-form solution is given by [10]

$$\boldsymbol{G} = \operatorname{sign}\left(\mathcal{H} \boldsymbol{\varphi} \right) \circ \max\left(\left| \mathcal{H} \boldsymbol{\varphi} \right| - \beta / \beta_0, 0 \right) . \tag{10}$$

$\circ$ denotes element-wise multiplication. After $\boldsymbol{G}$ and $\boldsymbol{\psi}_n$ are obtained, the $\boldsymbol{\varphi}$ sub-problem is pure-quadratic and can be solved by setting the derivative with respect to $\boldsymbol{\varphi}$ to zero, and the closed-form solution is given by

$$\boldsymbol{\varphi} = \frac{\sum\limits_{n=1}^{N} \boldsymbol{K}_n^T \left(\boldsymbol{s}_{n,dpc} + \alpha_0 \boldsymbol{\psi}_n \right) + \beta_0 \mathcal{H}^T \boldsymbol{G}}{\left(1 + \alpha_0 \right) \sum\limits_{n=1}^{N} \boldsymbol{K}_n^T \boldsymbol{K}_n + \beta_0 \mathcal{H}^T \mathcal{H}} , \tag{11}$$

where T denotes the transpose of a matrix. Since $\boldsymbol{K}$ and $\mathcal{H}$ are block-circulant and can be diagonalized by 2D Fourier transform, $\boldsymbol{\varphi}$ can be computed directly and only at the cost of the Fourier transform.

Algorithm 1: Half quadratic splitting for Eq. (7)

Input: DPC image $\boldsymbol{s}_{n,dpc}$, point spread function $\boldsymbol{K}_n$, penalty parameters α and β $\alpha_0 \leftarrow \alpha$, $\boldsymbol{\varphi} = 1$

While $\alpha_0 < \alpha_{\max}$ **do**

  Solving $\boldsymbol{\psi}_n$ sub-problem via Eq. (9) with given $\boldsymbol{\varphi}$

  $\beta_0 \leftarrow \beta$

  While $\beta_0 < \beta_{\max}$ **do**

    Solving $\boldsymbol{G}$ sub-problem via Eq. (10) with given $\boldsymbol{\varphi}$

    Solving $\boldsymbol{\varphi}$ sub-problem via Eq. (11) with given $\boldsymbol{\psi}_n$ and $\boldsymbol{G}$

    $\beta_0 \leftarrow a \cdot \beta_0$

  End while

  $\alpha_0 \leftarrow a \cdot \alpha_0$

End while

Output: Quantitative phase image $\boldsymbol{\varphi}$

To make the algorithm practically working well, a trick is to let and α_0 and β_0 increase in each iteration to gradually enforce $\left\| \boldsymbol{K}_n \boldsymbol{\varphi} - \boldsymbol{\psi}_n \right\|_2^2 \to 0$ and $\left\| \mathcal{H} \boldsymbol{\varphi} - \boldsymbol{G} \right\|_2^2 \to 0$, and the $\boldsymbol{\varphi}$, $\boldsymbol{\psi}_n$ and $\boldsymbol{G}$ are updated iteratively with known of each other.

In such a manner, the steps of the half quadratic splitting algorithm are sketched in **Algorithm 1**. In an actual implementation $a = 2$ by default. $\alpha_{\max} = 10^3$ and $\beta_{\max} = 10^5$ to ensure that α_0 and β_0 become large values.

4. EXPERIMENTAL STUDY

4.1 Simulation data

First we validated our algorithm on simulated data. System parameters were $\lambda = 0.530$ μm, $NA = 0.3$, a magnification of $\times 10$ and pixel size of the camera of 3.46 μm. A binary phantom object for the phase target is shown in Fig. 3 (a) where the phase is ranged in $[0, 2]$ rad.

According to the forward model, we generated 2 DPC-images corresponding to top-bottom illuminations and left-right illuminations and added Gaussian noises to them. The standard deviation of the Gaussian noise is $0.2\left(I_{\max} - I_{\min}\right)$, where $I_{\max}$ and $I_{\min}$ are the maximum and minimum values of each DPC image. Figure 3 (b) shows one of the DPC images where the image is severely corrupted by noise. The performance of our dsp-qDPC is compared against the following algorithms:

1) Tikhonov (L_2-norm) regularization-based qDPC (L_2-qDPC): we use the traditional qDPC reconstruction scheme by setting $\alpha = 0.0001$ in Eq. (1) with L_2-norm penalty that is

$$\boldsymbol{\varphi}_{L_2-qDPC} = \arg\min_{\boldsymbol{\varphi}} \sum_{n=1}^{N} \left\| \boldsymbol{K}_n \boldsymbol{\varphi} - \boldsymbol{s}_{n,dpc} \right\|_2^2 + \alpha \left\| \boldsymbol{\varphi} \right\|_2^2, \tag{12}$$

2) TV-regularization-based DPC (TV-qDPC): we use the gradient L_1-norm penalty function, and $\alpha = 0.1$

$$\boldsymbol{\varphi}_{TV-qDPC} = \arg\min_{\boldsymbol{\varphi}} \sum_{n=1}^{N} \left\| \boldsymbol{K}_n \boldsymbol{\varphi} - \boldsymbol{s}_{n,dpc} \right\|_2^2 + \alpha \left\| \nabla \boldsymbol{\varphi} \right\|_1. \tag{13}$$

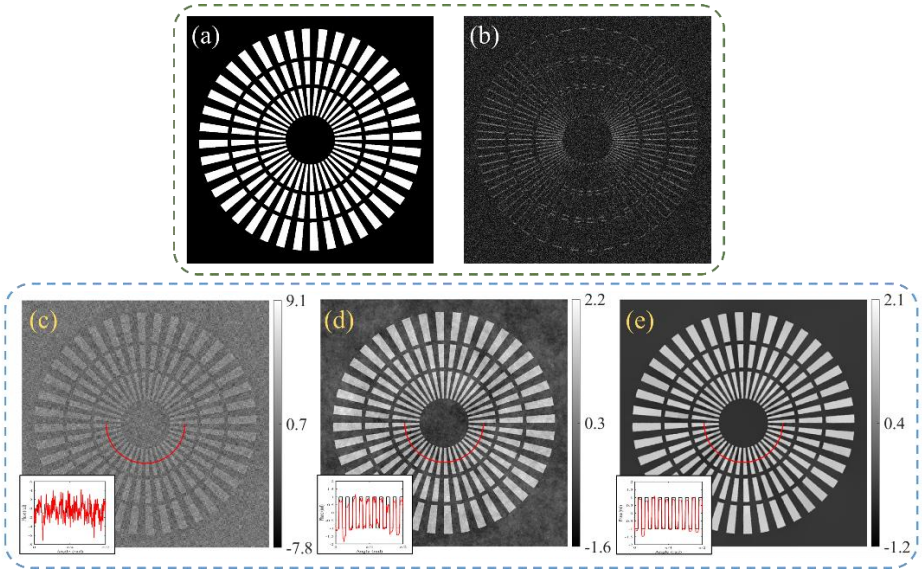

Fig. 2. Simulation of DPC reconstruction. (a) ground truth of the phase phantom. (b) The absolute value of DPC image corrupted by Gaussian noise. (c) Reconstruction results of L_2-qDPC. (d) Results of TV-qDPC. (e) Results of the proposed dsp-qDPC.

The reconstruction phase for L_2-norm regularization is shown in Fig. 2 (c). We also plot the phase value along the red curve in the black boxes to show the detailed comparison between reconstruction results and ground truth. According to Fig. 2 (c) and Fig. 2 (g), the noise signal is still very large and the algorithm fails to reconstruct the correct phase image.

Results of TV-qDPC are shown in Fig. 2 (d). The penalty parameter $\alpha = 0.123$. The TV regularization suppresses the impact of the noise signal as the reconstructed result approaches the ground truth as shown in Fig. 2 (a). However, the phase image is still corrupted by noise signals as the 'white-fog effects' are present in the background. Result of the

proposed dsp-qDPC, where $\alpha = 0.123$ and $\beta = 0.06$, is shown in Fig. 2 (e). According to Fig. 2 (e), the noise signal is significantly suppressed as there is no 'white-fog effects' in the background. Meanwhile, data fidelity is also guaranteed.

4.2 Real data

We validate our dsp-qDPC by imaging the unstained gastric cancer cells. The cells are imaged by an objective lens $NA = 0.3,\ \times 10$. The pixel size of the camera is 6.5 μm. The illumination wavelength is 532 nm. A region of interest (ROI) of size (1200 × 1200) is chosen as shown in Fig. 3 (a). The bright-field image has very low contrast, as the gastric cancer cells can be regarded as pure-phase objects.

As shown in Fig. 3 (b), the TV-DPC cannot suppress the 'white-fog' effect caused by uneven illumination fluctuation, while the dsp-qDPC significantly removes the 'white-fog' effect for the entire ROI as shown in Fig. 3 (c). Zoomed-in images listed in Figs. 3 (d1) to 3 (g3) show that our dsp-qDPC improves the reconstruction quality while maintaining the data fidelity, as the small structures such as the edges and branches of the cells are preserved.

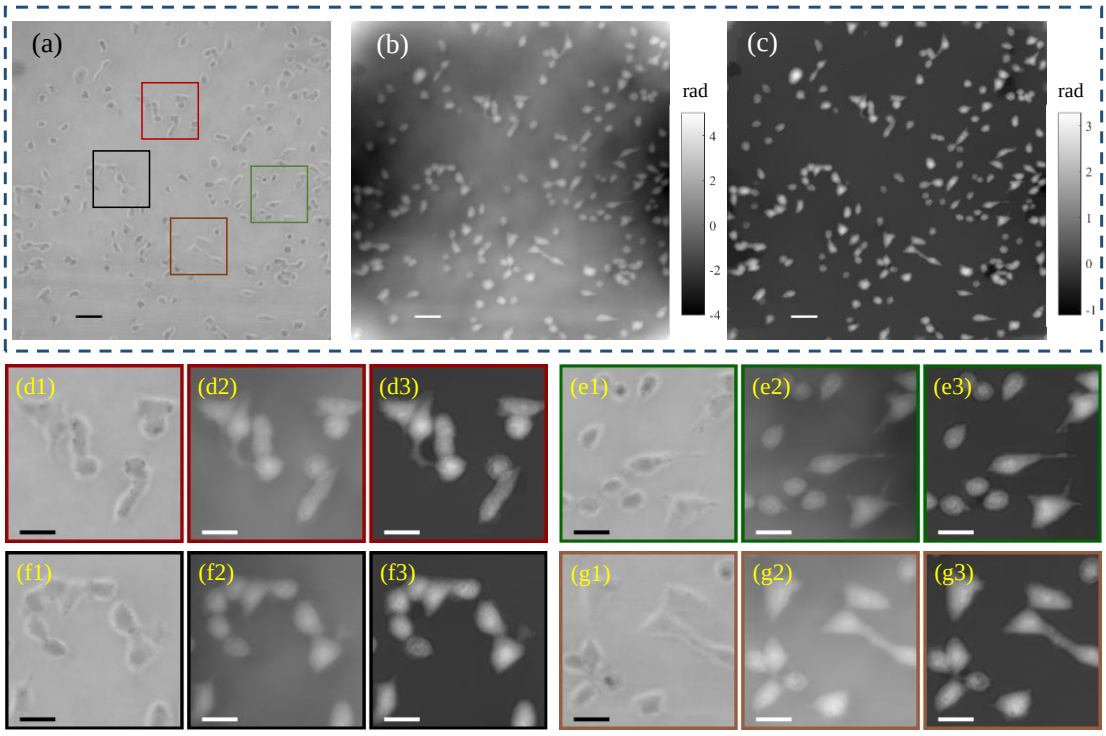

Fig. 3. Reconstruction results for gastric cancer cells. $\beta = \alpha = 0.01$. (a) Bright field image. (b) and (c) are recovery results using TV-qDPC and dsp-qDPC. Scale bar is 65 μm. (d1) to (g3) are zoomed-in images corresponding to the areas in the green, black, orange, and red boxes. Scale bar is 30 μm

We conducted tests of dsp-qDPC on color multiplexed single-shot DPC (cDPC) using HeLa cells as samples. The cells were illuminated by red, blue, and green colored LEDs and were imaged by an objective lens with $NA = 0.3,\ \times 10$. The pixel size of the camera is 5.85 μm. As shown in Fig. 4 (a), the input raw image for DPC reconstruction showed a phase contrast effect due to being illuminated by an oblique plane wave.

The DSP is a universal prior for qDPC image and it also works for cDPC as the 'white-fog' effect is suppressed shown in Fig. 4 (c). Zoomed-in images listed in Fig. 4 (d1) to 4 (g3) show that our dsp-qDPC improves the reconstruction quality where the clarity of the image is increased, and more delicate structures can be overserved.

Finally, we show that the dsp-qDPC benefits some potential applications using phase imaging, such as cell segmentation tasks (Automatic delineation of the cell boundaries). We applied Wang's method [12, 13] on both Fig. 4 (b) and Fig. 4 (c) with identical model parameters, and segmentation results are shown in Fig. 5. As shown in Figs. 5 (a1) to 5 (c1), the segmentation results on TV-qDPC output are not satisfactory due to lack of image contrast since the boundary signal of cells is reduced by the haze effect. Only a few cells are labeled as shown in Fig. 5 (c1). On the contrary, the segmentation results on dsp-qDCP are rather satisfactory where the boundary of the cells is recognized as shown in Fig. 5 (a2), and most of the cells are labeled as shown in Fig. 5 (c2).

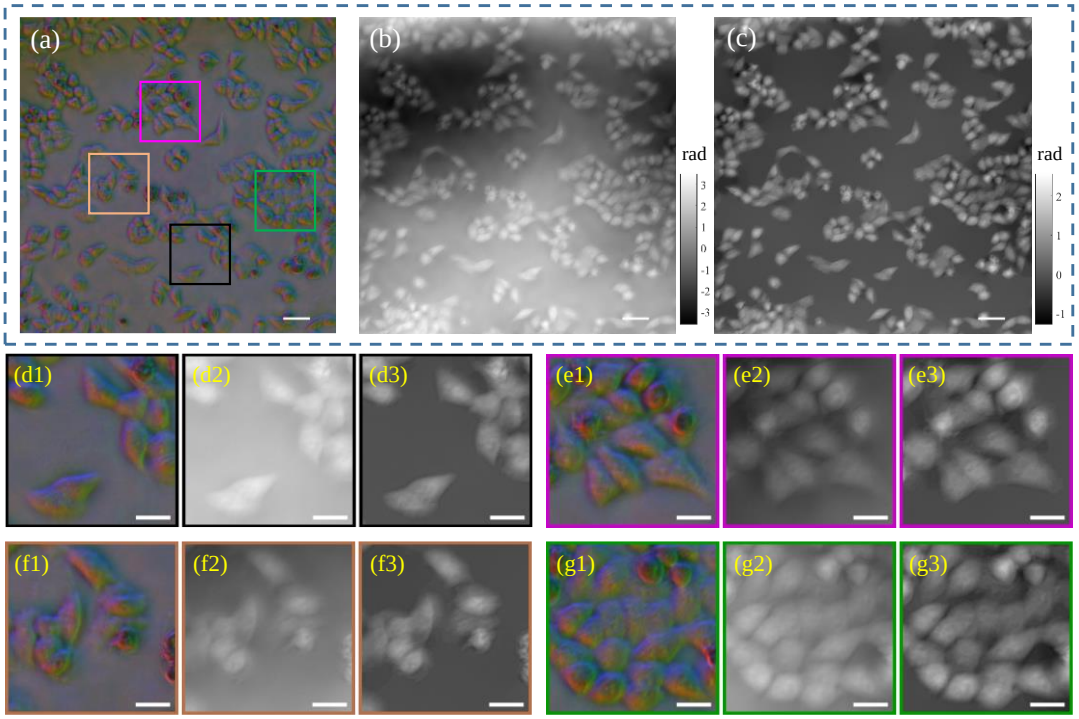

Fig. 4. Reconstruction results for HeLa cells using cDPC. $\beta = \alpha$. (a) Raw image for DPC reconstruction. (b) and (c) are recovery results using TV-qDPC and dsp-qDPC. Scale bar is 65 μm. (d1) to (g3) are zoomed-in images corresponding to the areas in the black, purple, orange, and green boxes. The scale bar is 30 μm.

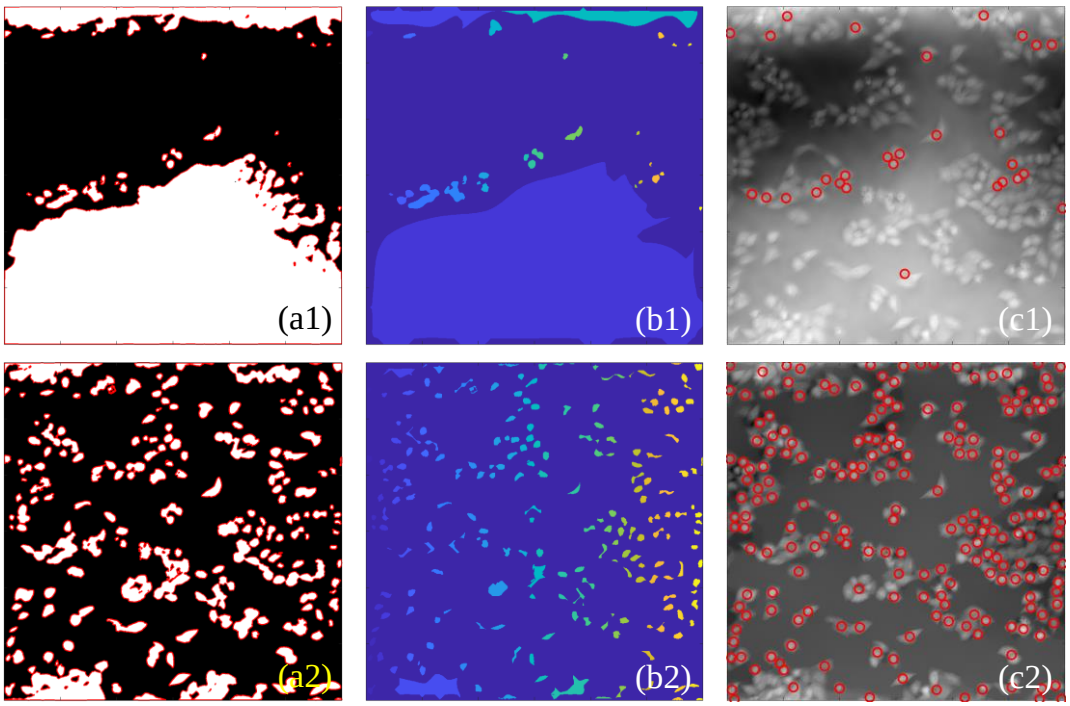

Fig. 5. Cell segmentation using phase image. (a1), (b1) and (c1) are boundary map, segmentation map, and counting map for image in Fig. 4 (b) (TV-qDPC). (a2), (b2) and (c2) are boundary map, segmentation map, and counting map for image in Fig. 4 (c) (dsp-qDPC).

5. CONCLUDING REMARKS

In this research, we proposed a new image prior – the dark-field sparse prior (DSP), and formulated a non-convex model to facilitate the quantitative differential phase contrast inverse problem. We use L_0-norm to represent the DSP and proposed to use HQS method to solve the NP-hard L_0-norm problem.

The DSP is effective because it has lower energy for idea DPC images than for noise-corrupted DPC images. The DSP favors the idea DPC images. As shown in Fig. 1(d), the idea DPC image is so sparser than the noise-corrupted DPC image that the DPC can simply distinguish the idea DPC image from that of noised DPC image. In this manner, the DSP gives lower energy to ideal DPC images, and rectifies the DPC deconvolution. The evolution of the phase output and latent image $\boldsymbol{K}_n\boldsymbol{\varphi}$ with respective to the iterations are shown in Video 1.

It is worth noting that our proposed dark-field spares prior can be extended beyond the DPC including but not limited to Fourier ptychography, and transport of intensity methods since the DSP is also a universal feature for optical images as long as dark-field measurements, or similar to dark-field are involved.

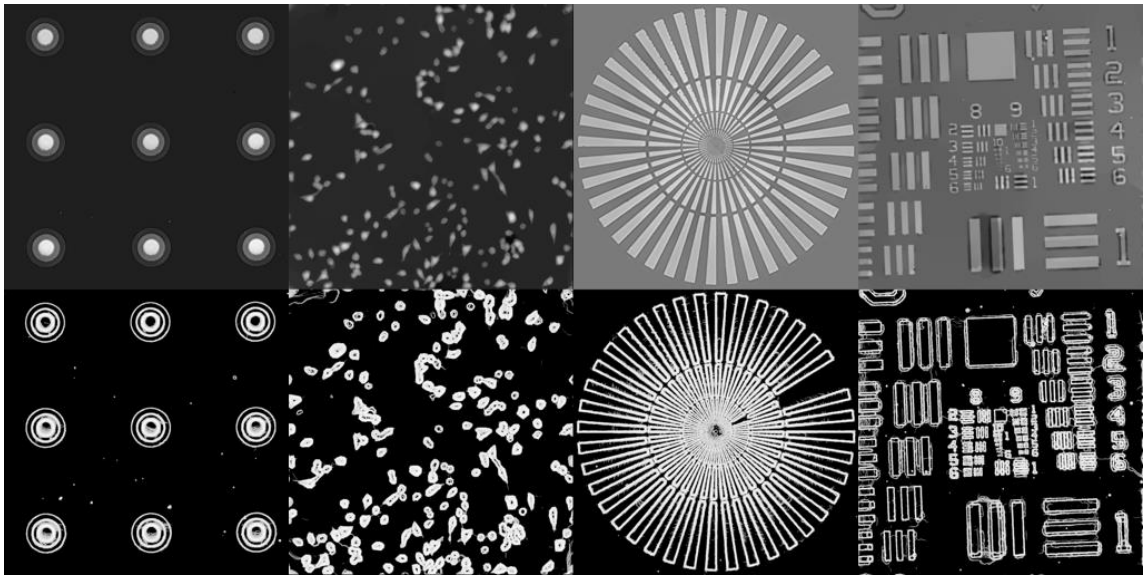

Video 1, Evolution of reconstructed phase pattern (upper row) and the latent image (lower row) with respective to iterations. http://dx.doi.org/10.1117/12.2683923.1

The limitation of dsp-qDPC includes the model parameters' tuning and computational efficiency. (1) Parameter α should be carefully selected to ensure that no image structure is eliminated by the hard-threshold operation in Eq. (9). An appropriate replacement for the hard-threshold operation, such as weighted soft-threshold, can be adopted to avoid such shortage. (2) The proposed HQS method involves large amounts of iteration before α_0 and β_0 reaching the $\alpha_{\max}$ and $\beta_{\max}$, the computational efficiency is not yet optimized. Using the split Bregman method [14] can further increase the computational speed of the dsp-qDPC.

REFERENCES

[1] D. K. Hamilton, and C. J. R. Sheppard, “Differential phase contrast in scanning optical microscopy,” Journal of Microscopy, 133(1), 27-39 (1984).

[2] C. W. See, M. V. Iravani, and H. K. Wickramasinghe, “Scanning differential phase contrast optical microscope: application to surface studies,” Applied Optics, 24(15), 2373-9 (1985).

[3] Liu, Xin, Guo *et al.*, “Visibility in differential phase-contrast imaging with partial coherence source,” Chinese Physics, (2007).

[4] S. B. Mehta, and C. J. R. Sheppard, “Quantitative phase-gradient imaging at high resolution with asymmetric illumination-based differential phase contrast,” Optics Letters, 34(13), 1924-1926 (2009).

[5] J. David Giese, T. N. Ford, and J. Mertz, “Fast volumetric phase-gradient imaging in thick samples,” Optics Express, 22(1), 1152-1162 (2014).

[6] L. Tian, and L. Waller, “Quantitative differential phase contrast imaging in an LED array microscope,” Optics Express, 23(9), 11394-11403 (2015).

[7] M. E. Kandel, C. Hu, G. Naseri Kouzehgarani *et al.*, “Epi-illumination gradient light interference microscopy for imaging opaque structures,” Nature Communications, 10(1), 4691 (2019).

[8] T. Laforest, M. Künzi, L. Kowalczuk *et al.*, “Transscleral optical phase imaging of the human retina,” Nature Photonics, 14(7), 439-445 (2020).

[9] D. Lee, S. Ryu, U. Kim *et al.*, “Color-coded LED microscopy for multi-contrast and quantitative phase-gradient imaging,” Biomedical Optics Express, (2015).

[10] Y. Wang, J. Yang, W. Yin *et al.*, “A new alternating minimization algorithm for total variation image reconstruction,” SIAM Journal on Imaging Sciences, 1(3), 248-272 (2008).

[11] L. Xu, C. Lu, Y. Xu *et al.*, "Image smoothing via L_0 gradient minimization." 1-12.

[12] Z. Wang, “A semi-automatic method for robust and efficient identification of neighboring muscle cells,” Pattern Recognition, 53, 300-312 (2016).

[13] Z. Wang, “A new approach for segmentation and quantification of cells or nanoparticles,” IEEE Transactions on Industrial Informatics, 12(3), 962-971 (2016).

[14] T. Goldstein, and S. Osher, “The split Bregman method for L1-regularized problems,” SIAM journal on imaging sciences, 2(2), 323-343 (2009).